Massachusetts Institute of Technology

Genetic control of aerogel and nanofoam properties, applied to Ni–MnO$_x$ cathode design

Tae-Gon Cha[1,2], Uyanga Tsedev[2,4], Alan Ransil[3,4], Amanda Embree[5], D. Benjamin Gordon[1,5], Angela M. Belcher[2,3,4]* and Christopher A. Voigt[1,2]*

[1] Synthetic Biology Center, Massachusetts Institute of Technology, Cambridge, MA 02139, USA

[2] Department of Biological Engineering, Massachusetts Institute of Technology, Cambridge, MA 02139, USA

[3] Department of Material Science and Engineering, Massachusetts Institute of Technology, Cambridge, MA 02139, USA

[4] Koch Institute for Integrative Cancer Research, Massachusetts Institute of Technology, Cambridge, MA 02139, USA

[5] MIT-Broad Foundry, Broad Institute of MIT and Harvard, Cambridge, MA 02139, USA

*Correspondence and requests for materials should be addressed to A.M.B. (belcher@mit.edu) or C.A.V. (cavoigt@gmail.com).

Abstract

Aerogels are ultralight porous materials whose matrix structure can be formed by interlinking 880 nm long M13 phage particles. In theory, changing the phage properties would alter the aerogel matrix, but attempting this using the current production system leads to heterogeneous lengths. We have designed a phagemid system that yields a narrow length distribution that can be tuned in 0.3 nm increments from 50 to 2,500 nm and, independently, the persistence length varied from 14 to 68 nm by mutating the coat protein. A robotic workflow that automates each step from DNA construction to aerogel synthesis is used to build 1,200 aerogels. This is applied to compare Ni–MnO$_x$ cathodes built using different matrixes, revealing a pareto-optimal relationship between performance metrics. This work demonstrates the application of genetic engineering to create "tuning knobs" to sweep through material parameter space; in this case, towards creating a physically strong and high-capacity battery.

2

Introduction

Aerogels are ultralight materials, sometimes referred to as "frozen smoke," whose properties are determined by the matrix chemistry and pore structure[1-7]. Their ultra-high surface areas and ultra-low densities make them ideal scaffolds to create nanomaterial composites with enhanced electrical conductivity and mechanical/thermal stabilities (carbon nanotubes, graphene, metal oxides, silica, etc.) [3, 6, 8-14]. These properties are ideal for battery components, such as cathodes or anodes, and the hierarchical porous structures of aerogels effectively accommodate any volume changes within electrodes during the charge-discharge process, impossible with traditional electrodes[11, 15-21]. As such, aerogel-based batteries have been explored for many battery chemistries, including lithium ion/metal/oxygen/sulfur/Te and sodium ion/oxygen[22-40]. Battery performance is dictated by the aerogel pore size and volume as well as the surface area, controlled by varying synthesis conditions; for example, acid concentration, solvents and gas pressure[24, 26, 28, 41-51].

Alternatively, aerogels can be templated by crosslinking M13 phage, which are linear 880 nm rods[52]. M13-templated porous structures have been used for various applications, including batteries, solar cells, catalysts, and imaging[53-59]. Aerogels built from M13 phage have densities between 2-5 mg/cm^3 and porosities as high as 99%[52]. The wild-type phage consists of a packed genome surrounded by an external shell of 2,700 copies of the pVIII protein. pVIII has been mutated to alter charge, add binding sites for metals or nanomaterials, or enable protein-protein interactions to direct their self-assembly into defined structures[54, 60-70]. The addition of an N-terminal EEAE to pVIII increases the negative surface charge, which enhances the material nucleation and metal deposition onto the surface of the phage scaffolds[71-73]. Phage flexibility can be changed my mutating pVIII (Y21M), which increases the persistence length and inverts the pVIII helix chirality from left- to right-handed[74].

So-called phagemid systems are used to produce the phage particles required for material synthesis[75-78]. Phagemids are plasmids containing one or two f1-oris that replicate single-stranded DNA (ssDNA) in the presence of phage proteins, expressed by helper phages or plasmids in *Escherichia coli* [79-80]. The replication of ssDNA proceeds following a rolling circle mechanism in the presence of pII, a phage protein that binds to specific sequence sites in f1-ori (nicking region – TTTAATA, β – TGGAC, γ – GTTCCA, δ – TGGAAC) and induces a single strand break at the nicking site[81]. The free 3'-hydroxyl end of the nick serves as a primer for ssDNA synthesis, which proceeds through displacement of the nicked strand as ssDNA by DNA polymerase III and the *rep* helicase in the presence of single stranded DNA binding protein (SSB)[82-83]. ssDNA replication terminates by pII cleavage of ssDNA at a second downstream nicking site[84]. The ssDNA is circularized, bound by pV proteins for transport to the cell membrane, and wrapped by the major phage coat and capsid proteins during extrusion of the phage particle. The phage length is determined by the size of the packaged ssDNA[85]. Fine control over the size of the packaged ssDNA was previously attempted by flanking the desired sequence length, containing a packaging signal (PS), between a full f1-ori and a truncated f1-oriΔ29, which was designed to terminate replication[86-90]. In this way, various groups have showed that the phage can be shortened to as little as 50 nm (~95 pVIII copies) and lengthened to 1,300 nm[88, 91]. The challenge is that the underlying populations are bimodal because unintended longer "genomes" are produced by the ssDNA starting at f1-oriΔ29 and ending at f1-ori. Phages produced from the f1-ori/f1-oriΔ29 system require an additional purification step to ensure uniform length phage batches, thus compromising the inherent scalability of the phage amplification process for downstream material applications.

Here, we present a phage production system that generates uniform phages with precisely controllable length and a high-throughput pipeline for their conversion to aerogels and the determination of material properties. This is achieved by modifying f1-ori and f1-oriΔ29 to block the readthrough of DNA polymerase. This yielded a unimodal distribution of phage lengths that can be varied from 50 nm to 2,500 nm. Further, the persistence length can be varied up to 5-fold by making different amino acid substitutions to pVIII residue 21. Using automated liquid handling we can co-

4

transform phagemid/helper plasmids into *E. coli*, produce phages, purify them, make phage-hydrogels, lyophilize hydrogels to make aerogels and characterize them, all in high-throughput (~1,000/week). Based on the measured aerogel properties, we selected five phage lengths to make Ni–MnO$_x$ cathodes, a promising material for lithium ion batteries due to its low cost and non-toxicity[92-95]. The cathodes are produced by forming phage hydrogels that are converted to Ni nanofoams on which MnO$_x$ is deposited[96-97]. By changing phage length and stiffness, we are able to control porosity, battery performance and mechanical strength of the resulting cathode. The conditions for creating these materials are identical and the properties are tuned solely through the genetic manipulation of the phage.

Results

Phagemid engineering to generate uniform phage

The phage production system is based on *E. coli* K561 harboring the phagemid and helper phage R474[91]. The phagemid contains the DNA sequence to be packaged, located between two f1-ori sequences that are intended to initiate or terminate ssDNA production (Figure 1a). Internal to the ssDNA sequence, the hairpin packaging signal (PS) structure is included to ensure recognition and encapsulation of the ssDNA by the assembly proteins encoded by the helper plasmid[98]. With this design, we find that the wild-type f1-ori signal (146 bp) both initiated and terminated ssDNA production, whereas the f1-oriΔ29 (86 bp) terminated replication and also allowed some level of replication initiation, resulting in unwanted side products (Figures 1b-c).

Our starting phagemid (EP475) contained 561 bp of DNA from the natural phage genome M13KE[99]. The construct was intended to generate 475 bp ssDNA (including the PS sequence) for the assembly of 100 nm phages. We quantified the population of phage sizes produced using this system. Transmission electron microscopy (TEM) images were taken, from which the phage lengths were measured (Figures 1c-f) (Methods). About one third of the phage were in the expected range of

lengths (average = 97 nm), corresponding to the ssDNA produced from replication starting at f1-ori and ending at f1-oriΔ29 (475 bp). However, the remaining two thirds of the phage population was found to be much longer with an average length of 620 nm, which corresponds to the packaging of ssDNA initiated at f1-oriΔ29 and terminated at f1-ori (4422 bp). Note that longer phages are assembled despite the lack of a defined PS in this region. To confirm the origin of this population of longer phage, we designed another phagemid (EP1960) to package a larger sequence of 1960 bases. This again resulted in a mixed phage distribution centered at 310 nm and at 680 nm (Supplementary Figure 1). Therefore, we concluded that this was due to replication initiated at f1-oriΔ29 and not due to the formation of polyphages or phages produced from multiple, serial incorporation of ssDNA[86].

To correct this problem, we first designed a novel phagemid system by modifying the f1-ori to create versions that only initiate (f1-α) and only terminate (f1-δΔ29) ssDNA production. To make f1-α, the 10 bp α sequence (AGTCC ACGTT) required for termination is deleted[100]. When this sequence is used for initiation (EP475α), a bimodal population remains, but the percent of phage that are the correct length improves from 31% to 86% (Supplementary Figure 2). This improvement is the result of incorrect replication of ssDNA from f1-oriΔ29 being unable to terminate at f1-α, thus decreasing production efficiency of incorrect phage. Still, 10% of the phage are the length of the incorrect sequence, indicating that the f1-α sequence still retains some ability to terminate.

Next, we created a version of f1-oriΔ29 that terminates but is not able to initiate. Viral genome replication occurs after the f1-ori sequence binds to pII proteins and is nicked[101]. There are four pII binding sites (nicking site, β, γ and δ) and binding between four pII proteins and these sites induces conformation changes that promote nicking of the (+) strand (Figure 1b). We sequentially tested alternative f1-oriΔ29 sequences where each of these sites was deleted (Supplementary Figure 2). We found that the removal of the δ site (f1-δΔ29), combined with f1-α to create EP475αδ, yielded the largest percent of correct phage (95%) with no distinct subpopulation at a different phage length (Figures 1e-f).

6

Genetic control of phage length and stiffness

With the improved f1-α/f1-$\delta\Delta$29 system, phage length is controlled by changing the DNA length between the f1-α initiator and the f1-$\delta\Delta$29 terminator (Figure 2a). A set of thirteen phagemids were designed that where this DNA ranges from 330 to 19,800 bp, all containing a PS[98]. The non-PS "inactive" remainder of the ssDNA was filled in using a DNA sequence we had previously observed to be inactive in *E. coli*[102]. These phagemids lead to uniform length distributions between 50 to 2,500 nm (with an average standard deviation of ± 5%) (Figure 2b and Supplementary Figure 3). There is a linear correlation of phage length *L* with the ssDNA size *n* that follows $L = 0.13\ n$ (Figure 2c). Note that phagemids with a single wild-type f1-ori can also lead to uniform distributions, but the length cannot be reduced to <200 nm because of additional required DNA in the plasmid backbone (ori and antibiotic resistance) (Supplementary Figure 4).

The pVIII Y21M mutation has been reported to stiffen *fd* phage from a persistence length of 2.8 μm to 9.9 μm (for 10 μm long multimers)[74]. We mutated this position on the M13 pVIII protein to all 20 amino acids and measured the impact on the persistence length for this smaller phage (Figure 2d) (Methods). The phage produced by each pVIII mutant with EP475$\alpha\delta$ (100 nm phage) were purified and the hydrodynamic radiuses measured using dynamic light scattering (DLS). From this, the persistence length can be calculated assuming the phage particle behaves as a wormlike chain and using the phage length measured from TEM images (Methods). This method has been used to estimate the persistence length of rod-shaped biomolecules, including DNA[103]. The persistence lengths of the mutant 100 nm phages range from 14 to 68 nm, without affecting length (Figure 2e and Supplementary Figure 5). The Y21M mutation only showed a 50% increase in persistence length when introduced in M13 phage, in contrast to the larger effect observed for *fd* phage.

7

Automated workflow for aerogel creation

Lab automation protocols were developed to encompass all steps from plasmid transformation into *E. coli* to aerogel formation (Supplementary Figure 6). The creation of phages of different lengths and stiffnesses was simplified by having each property encoded in separate phagemids and helper plasmids that can be co-transformed. To this end, 60 phagemids were constructed containing DNA sequences ranging from 330 to 19,800 bp in increments of 330 bp (Supplementary Table 2). These were co-transformed together with the 20 helper plasmids, each coding for a different pVIII mutant. The 1,200 strains were constructed using Echo and Mantis liquid handlers to mix the plasmids/cells and transformations were performed in 96-well format using Bravo and Hamilton automated handling systems (the detailed workflow is described in the Methods) (Figure 3a and Supplementary Figure 6). After transformation, cells were plated using the Hamilton, incubated and then picked into 96 deep-well plates (1.3 mL of 2xYT media instead of LB media to increase phage titer (Supplementary Figure 7)) using a colony picker (Supplementary Figure 6). The culture was grown, cells removed by centrifugation, and then PEG/NaCl was added using the Hamilton to precipitate the phage from the growth media. The precipitated phage pellets were then re-dispersed in water. Typically, 10^{13} phage particles were produced through this workflow and they follow the same length distribution as obtained from low-throughput techniques (Supplementary Figure 8).

Aerogels were synthesized from the phage variants using the Hamilton to deposit them on hydrophobic glass slides that are then heated at 50 °C for 30 min to increase phage concentration past the critical point (0.08 wt%) where phage particles interlink through Van der Waals forces[104]. The interlinked phage form a hydrogel that was then converted to an aerogel using the freeze drying method[52]. The resulting material had the highly-porous structural characteristic of aerogels (Figure 3b).

The mechanical strengths (Young's moduli, *E*) of the aerogels were measured using atomic force microscopy (AFM)[105-106]. A force displacement curve can be plotted from indentation at a single point on the phage-aerogel surface by the AFM tip in contact mode (Figure 3c). Using the

Hertzian model[107], the E of an aerogel can be calculated from the force-displacement curve assuming a Poisson ratio of 0.5, which is consistent with biomaterials (Figure 3c). Because AFM is difficult to automate, a subset of 300 variant samples was selected and their E measured (Figure 3d). The aerogels produced from smaller and more rigid phage tend to produce stiffer aerogels, with a 6-fold range in E observed over the complete set (Figures 3e-f). These results are consistent with numerical simulations predicting particle size effects on the mechanical properties of silica aerogels[108-109] and has been experimentally observed for other porous nanomaterials[110-112].

Genetic optimization of structural battery electrodes

High-performance structural batteries rely on simultaneous optimization of coupled electrochemical and mechanical properties, and we therefore sought to determine whether these properties could be controlled and co-optimized using phage genetics. Biotemplated nickel aerogels were produced from genetically modified phage and employed as current collectors by electrodepositing an active material in order to produce robust Ni–MnO$_x$ biotemplated nanofoam electrodes. Different phage lengths were selected from our subset: 320, 430, 550, 750, 960, and 1,300 nm (all pVIII-EEAE Y21). Biotemplated metal nanofoam current collectors were constructed following a previously-reported protocol[96, 113-114]. Briefly, the phages are chemically crosslinked with glutaraldehyde to form hydrogels onto which nickel is deposited first using an electroless deposition solution followed by the electrodeposition of a manganese oxide active material (Figure 4a) (Methods). The effect of heat treatment was assessed using thermogravimetric analysis (Supplementary Figure 9).

Materials produced using phage of different length and stiffness but identical processing conditions were evaluated (Figure 4b). Scanning electron microscope (SEM) images reveal that nanofoams templated phages exhibit distinct morphologies. This variation was quantified in order to assess the effect of phage genetics on foam porosity. Foam porosity was quantified from the SEM images, showing that an intermediate phage length (750 nm) yielded the maximum porosity (Figure

9

4c).

Batteries were constructed using the biotemplated Ni–MnO$_x$ electrodes as cathodes. The batteries were assembled using lithium foil as the negative electrode, a celgard separator and an electrolyte consisting of 1M LiPF$_6$ in EC:DMC (Methods). The rate capability of the electrodes was determined by electrochemically cycling batteries using different currents, showing how rapidly a battery charge or discharge. The active material mass was calculated by weighing dry electrodes both before and after active material deposition, and nominal capacity upon discharge was calculated by dividing the electrochemical discharge capacity measured during cycling by these active material mass. Typical discharge curves are shown in Supplementary Figure 10 . These exhibit a discharge capacity up to 135 mAh/g similar to previous published manganese oxide data[115-117]. First cycle coulombic efficiencies are given in Supplementary Figure 11, and are high due to organic residues. However, cycling data shown in Supplementary Figure 12 show stability for 20 cycles. Electrodes made using higher porosity nanofoams show a shoulder near 2.8 V corresponding to manganese oxide intercalation. Electrodes based on lower porosity samples, by contrast, show a sloped capacitive behavior with no shoulder. This indicates that intercalation plays less of a role in electrochemical cycling when the porosity is low. This would be expected if lithium diffusion through the liquid electrolyte is blocked due to lower sample porosity. This effect of biologically controlled porosity on electrode rate capability was assessed by Ragone plots of batteries using phage of different lengths (Supplementary Figure 13). Low rates result in higher capacity for all electrodes. The strong effect of porosity on rate capability in these batteries indicates that these electrodes contain electrochemically inaccessible active material.

Figure 4e shows the measured nominal capacity as a function of the length of the phage used to make the biotemplated electrode. It follows the same trend as the porosity of the material, including an optimum at 750 nm. The peak value of 121 mAh/g is similar to the theoretical maximum capacity of the manganese oxide active material of 147 mAh/g, indicating an 82% active material utilization. Because the active chemistry is the same for these materials, these data indicate that the

morphology changes the lithium ion transport through the liquid electrolyte. Materials with lower porosity contain a lower volume fraction of liquid electrolyte, resulting in a corresponding rate limitation due to lithium diffusion constraints.

The mechanical strengths of the cathodes were measured using AFM (Figure 4f). There is a general trend of smaller phage leading to mechanically-stronger materials, similar to the relationship between phage length and mechanical strength for the aerogels (Figure 3e). However, there is an optimum E for the cathode biotemplated by 430 nm phage (Figure 4f). This reveals the competing needs of a structural battery to have high mechanical strength, requiring robust scaffolds, and high capacity, which requires that the foam be highly porous. Using phage of different length, we can identify the optimum in balancing both of these constraints, which for our system is the biotemplated cathodes produced using 750 nm phage.

Discussion

Our system encodes the structural features of an aerogel or hydrogel in the genetics of the scaffolding phage. Mutations can then be made to sweep through material properties without changing the chemistry or processing conditions. As an 880 nm rod, the geometry of M13 phage has proven valuable to scaffold an enormous range of materials, including batteries, catalysis, photovoltaic cells, sensors, and optical tools[118]. Control over the rod length and stiffness paves the way for the exploration of new regions of the phage materials space, with potential new functional properties, but previous efforts have led to mixed populations that lead to heterogenous materials. With the newly designed phagemid/helper plasmid system (f1-α/f1-$\delta\Delta$29) and automation of the material construction process, we are able to access new parameters for phage templated material development. We can sweep through the gel porosities and scaffold morphologies to identify optimal materials for the target application. Porosity control is critical for many applications of phage-templated materials, including flexible electrodes, filtration membranes and drug delivery

11

systems[119-122]. Control over the metal nanowire morphology in the material is essential for photonic/electronic nanodevices and biomedical sensors[123-124].

Here, phage genetic control used to create cathodes that balance the competing needs for high capacity (highly porous) with mechanical strength (robust scaffolding). The optimal phage-templated Ni–MnO$_x$ cathode using 750 nm phages have ~120 mAh/g of nominal capacity as well as ~20 MPa of Young's modulus. The capacity of the cathode is competitive compared to other cathodes of lithium ion batteries[125]. On the other hand, the Young's modulus of cathode is lower than minimum value (~1 GPa) needed to structure panels of battery material[126]. However, using stiffer phages as a template could improve mechanical strengths of the materials as the cathode made by engineered phage with Y21A pVIII (exhibited ~2.4 times higher Young's modulus that made by wild-type phage). Incorporation of strong metallic materials to the phage templates may additionally enhance the mechanical strength. Our ability to genetically manipulate the filament properties of phages can be used to optimally design for structural batteries that are able to carry a mechanical load as well as efficiently store electrical energy, with the ultimate objective of eliminating the need for a conventional battery by replacing it with multifunctional body panels[127-128].

Our length-controlled phage have several advantages over abiological methods to create porous nanomaterials. They provide higher mono-dispersity and uniformity compared to the commercially-available polymeric particles or carbon-based nanoparticles[129-131]. The crystal packing of M13 phage is 4 nm with evenly spaced nucleation events that gives small and uniform particles sizes. In addition, the proteins of phage can be easily engineered by adding specific peptides, which allows us to attach various metal ions or organic/inorganic materials uniformly on the surfaces of M13 phage[132-134]. Furthermore, the phage is easily crosslinked with servers to form filaments, which allows us not to add any additives in the cathode synthesis. The disadvantage of using phage is the ability to scale-up for the production of bulk materials. Several companies have been able to scale phage production through fermentation to multi-kilogram scales. Another approach is to use what is

12

learned from the phage materials to direct the synthesis of an abiological version that is easier to scale. An example of this was demonstrated by Cambrios, where silver nanowires for touch screens, phones and all-in-one computers were initially discovered using phage and then reconstructed for bulk production by Huawei. To this end, our ability to control phage properties allows for the systematic screening of thousands of materials with altered properties, beyond that which is easily accessible through chemical techniques.

Methods

Strains, plasmids, and culture media. Chemically competent *E. coli* XL1-Blue (*recA1 endA1 gyrA96 thi-1 hsdR17 supE44 relA1 lac* [F′ *proAB lacI^qZΔM15* Tn*10* (Tet^r)]) (Agilent Technologies, 200249) was used for all molecular cloning and phage production experiments. Chemically competent cells were purchased or made using the Mix & Go *E. coli* Transformation Kit (Zymo Research, T3001). All *E. coli* strains were grown at 37 °C in LB-Miller media (BD Biosciences, 244620) and LB/agar plates (1.5% of Bacto Agar (BD Bioscience, 214010) unless otherwise indicated. The engineered phagemids were derived from the plasmid pLS7[74], and the helper plasmid M13-f1 was constructed based on M13mp18[135]. The sequence and detailed plasmid map are provided in Supplementary Table 1 and Supplementary Figure 14. The following concentrations of antibiotics were added to maintain plasmids in liquid cultures and plates: 100 μg mL^-1 ampicillin (GoldBio, CAS#69-52-3), 40 μg mL^-1 tetracycline (GoldBio, CAS#64-75-5) and 50 μg mL^-1 kanamycin (GoldBio, CAS#25389-94-0).

Low-throughput phage production and purification. *E. coli* is first transformed with the phagemid and helper plasmid. Cells are then streaked on LB/agar plates with ampicillin and kanamycin and grown at 37 °C overnight. The single colonies were inoculated in 70 mL of LB media with ampicillin and kanamycin and grown in 250 mL Erlenmeyer flasks at 37 °C and 250 r.p.m. in a New Brunswick Innova 44 shaker-incubator overnight. The cultures were transferred to a 250 mL

Nalgene PPCO centrifuge bottle (Thermo Scientific, 3120-0250) and centrifuged at 10,000 g at 4 °C for 30 min in a Sorvall RC 6+ centrifuge (Thermo Scientific) with the Fiberlite F14-6 x 250y fixed angle rotor (Thermo Scientific, 78500) and the supernatant containing phage was collected. To purify the phage, 20 mL 50% (w/v) PEG8000 (Sigma Aldrich, 89510) and 10 mL 5M NaCl (Sigma Aldrich, S3014) were added to the collected phage solution. The phage mixtures were incubated at 4 °C for 24 hr and then centrifuged at 20,000 g at 4 °C for 30 min. After gently removing the supernatant, the phage-PEG/NaCl precipitations were re-dispersed vigorously in 2 mL of 1X TBS buffer (Sigma Aldrich, T5912 diluted 10x into DI water). To remove cell debris and extra PEG/NaCl, the solutions were transferred to pre-chilled 2.0 mL microcentrifuge tubes (VWR, 20170-170) and centrifuged at 15,000 r.p.m. at 4 °C for 30 min in a refrigerated benchtop Eppendorf Centrifuge 5424R (Eppendorf, 540400138) and the supernatants were collected and hereafter referred to as the "phage solution". This protocol was used for the data shown in Figures 1 and 2.

Transmission Electron Microscopy.   A 10 μL aliquot of phage solution was deposited on a 200-mesh formvar/carbon-coated copper TEM grid (Electron Microscopy Sciences, FCF200-Cu). The spot was allowed to rest for 3 min and then the excess liquid was removed using a Kimwipe. The phages were stained using 10 μL of 1% uranyl acetate alternative (Gadolinium Triacetate, Ted Pella, 19485) that is deposited on the TEM grid and allowed to rest for 20 min. The excess stain solution was removed using a Kimwipe. High-resolution TEM (JEOL 2010) was performed at 200 kV accelerating voltage (Electron Microscopy lab at the Center for Materials Science and Engineering CMSE, MIT). The images were collected at 15000x magnification for lengths EP330$\alpha\delta$ to EP5280$\alpha\delta$ and 10000x magnification for lengths EP6600$\alpha\delta$ to EP19800$\alpha\delta$. To quantify phage length, the TEM images were analyzed using ImageJ software. For each phage the line was manually drawn along the phage, and then the "Measure" command was used to measure the line length. The histograms were drawn by randomly sampling 198 phage particles produced from phagemids EP475, EP1960, EP475α, EP475$\alpha\beta$, EP475$\alpha\gamma$, and EP475$\alpha\delta$ and the remaining histograms were drawn by randomly sampling 99 phage

particles. The experiments were performed as three replicates where bacterial growth was initiated on different days and even numbers of phage particles were selected from each replicate (*e.g.*, the 99 particles come from 3 replicates and 33 particles from each replicate).

Dynamic Light Scattering.   Dynamic light scattering was performed using a cuvette-based DLS instrument (Wyatt Technology Corporation, DynaPro NanoStar). A 450 μL aliquot of phage solution was pipetted into a plastic cuvette (Eppendorf, 952010069) and the hydrodynamic radius $<R^2>$ of phage was measured. The persistence length *P* was calculated[103] considering $<R^2>$ and the phage length *L*, according to $<R^2> = 2LP - 2P^2(1 - e^{-L/P})$.

Phage-to-aerogel Workflow.   To construct the 1,200 strains, 60 phagemids and 20 helper plasmids were mixed in a 96-well PCR plate (Thermo Scientific, AB-800) using the Echo 550 acoustic liquid handler (Labcyte) and the Echo Cherry Pick software. A 10 μL aliquot of chemically-competent *E. coli* XL1-Blue (Agilent Technologies, 200249 or made in our laboratory) was added to each well using a Mantis liquid handler (Formulatrix). A thermocycler (Bio-Rad C1000 Touch) was used to heat shock the cells at 42 °C for 35 s. Cell mixtures were recovered using 70 μL of SOC outgrowth media (New England BioLabs, B9020S) added using a Bravo automated liquid handling platform (Agilent). After incubating at 37 °C for 60 min, the cells were transferred to 24 channel LB/agar trough plates (Analytical Sales and Services, Inc., 47025) with ampicillin and kanamycin using a Hamilton Microlab STAR liquid handling system (Hamilton). The plates were incubated at 37 °C for 2 days. The single colonies were inoculated in 96 deep well plates (Southern Labware, 503501) (in 1.3 mL of 2xYT media (BD Biosciences, 244020)) using Rapid Complete Colony Picker (Hudson Robotics) and incubated at 37 °C and 250 r.p.m. overnight in a Multitron Pro shaker-incubator (INFORS HT). To remove *E. coli* cells, the 96 deep well plates were centrifuged at 4,000 g and 4 °C for 30 min in a Sorvall Legend XFR centrifuge. A 700 μL aliquot of supernatant was transferred to another 96 deep

well plate and mixed with 200 µL of 50% (w/v) PEG8000 and 100 µL of 5M NaCl using the Hamilton Microlab STAR liquid handling system (Hamilton). The cell mixtures were incubated at 4 °C for 24 hr in a refrigerator. The 96 deep well plates were centrifuged at 4,000 g for 30 min and then the supernatant was removed gently. The phage-PEG/NaCl pellets were re-dissolved in 100 µL of DI water, added using a Hamilton Microlab STAR liquid handling system (Hamilton). To remove debris, the 96 well plates were centrifuged at 4,000 g and 4 °C for 30 min in a Sorvall Legend XFR centrifuge and 50 µL of the supernatant were transferred to a new 96 deep well plates using Hamilton Microlab STAR liquid handling system (Hamilton).

Aerogel synthesis. The protocol was adapted from one previously published[52]. Briefly, for each sample, a 50 µL aliquot of 0.02 wt% of phage was pipetted onto a hydrophobic printed well slide (Fisher Scientific, 12-580-23) using the Microlab STAR liquid handling system (Hamilton). The slides were heated at 55 °C for 30 min to concentrate the phage solution through evaporation. Three-dimensional gel networks were formed at 0.08 wt.% of phage. The slides were lyophilized for 30 min in a freeze dryer (Labconco) for 30 min to transform the gel network into an aerogel.

Scanning Electron Microscope. Sample slides were first coated with thin Au films using an Au sputter coater in a vacuum (Quorum Technologies, SC7640). SEM images were obtained at randomly chosen locations using SEM (JEOL 6010 LA, JEOL) with a tungsten lament. The beam voltage was set to 20 kV and samples were investigated in secondary electron imaging (SEI) mode.

Atomic Force Microscope. A Veeco Dimension 3100 AFM was used with a four-sided pyramid contact AFM Si cantilever tip (Bruker, MLCT, k = 0.01 N/m). After indentation of AFM tip to the surfaces of aerogels, Ni nanofoams and Ni–MnO$_x$ cathodes, the force-displacement curves were

obtained. E is calculated using the Hertzian model, $F = E (1-\nu^2)^{-1}(\tan \alpha)2^{-0.5}\delta^2$, where F is total force, ν is Poisson's ratio (0.5 for phage-aerogel[136-137], 0.30 for Ni nanofoams[138], and 0.27 for Ni–MnO$_x$ cathodes[138]), α is edge angle of cantilever tips (15.0° for MLCT AFM tips), and δ is total displacement. For each sample, five data points were measured at the different positions and then averaged to obtain Young's modulus.

Phage production and purification for metal nanofoams. The protocol differs slightly than that described above for the production of nanofoams. After phagemid/plasmid co-transformation and overnight growth, the single colonies were inoculated in 700 mL of LB media with ampicillin and kanamycin and grown in 2,800 mL Erlenmeyer flasks (Sigma-Aldrich, CLS44202XL) at 37 °C and 250 r.p.m. in a New Brunswick Innova 44 shaker-incubator overnight. The cultures were transferred to a 1,000 mL Nalgene PPCO centrifuge bottle (Thermo Scientific, 3120-1010) and centrifuged at 10,000 g at 4 °C for 30 min in a Sorvall RC 6+ centrifuge with a Fiberlite F10-4 x 1000 fixed angle rotor (Thermo Scientific, 096-041053), after which the phage supernatant was collected. To purify the phage, 200 mL of 50% (w/v) PEG8000 and 100 mL 5M NaCl were added to the phage supernatant. The samples were then incubated at 4 °C for 24 hr and then divided into six samples, which were transferred to 250 mL Nalgene PPCO centrifuge bottles (Thermo Scientific, 3120-0250) and centrifuged at 20,000 g at 4 °C for 30 min. After gently removing the supernatant, the phage-PEG/NaCl precipitations were re-dispersed vigorously into 7 mL of 1X TBS buffer (each bottle). All re-dispersed phage mixtures were transferred to 100 mL round media storage bottles (Corning, 1395-100). As a 2nd purification step, 12 mL of 50% (w/v) PEG8000 and 6 mL 5M NaCl were added to the collected phage solution. The phage mixtures were incubated at 4 °C for 24 hr and then divided into two samples and transferred to Nalgene high-speed PPCO centrifuge tubes (Thermo Scientific, 3119-0050PK) and centrifuged at 20,000 g at 4 °C for 30 min in a Sorvall RC 6+ centrifuge with the Fiberlite F21S-8 x 50y fixed angle rotor (Thermo Scientific, 46923). After gently removing the supernatant, the resulting phage pellets were re-suspended in 2 mL of 1x PBS buffer (Gibco, 10010023). To remove

cell debris and excess PEG/NaCl, the solutions were transferred to pre-chilled 2.0 mL microcentrifuge tubes and centrifuged at 15,000 r.p.m. at 4 °C for 30 min in a refrigerated benchtop Eppendorf Centrifuge 5424R. The supernatants were then collected, which contained ~10^{13} phage/mL.

Measurement of phage concentration, weight, and titer. The concentration of the phage solution was determined by measuring the OD at 269 nm and OD at 320 nm using an UV-Vis spectrophotometer (Nanodrop, ND-1000). The difference between OD_{269nm} and OD_{320nm} reflects the absorbance of phage particles at 269 nm[139]. The concentration *c* is calculated using Beer's law (c = $A\varepsilon^{-1}l^{-1}$) where *A* is the absorption (OD_{269} – OD_{320}), ε is the extinction coefficient of phage at 269 nm (3.84 mL mg^{-1} cm^{-1})[140] and *l* is the light path of the UV-Vis spectrophotometer (1 mm). The phage mass was calculated by multiplying the concentration by the volume of phage solution. The number of phage particles was derived from the concentration *c* using $cMW_{phage}^{-1}N_A^{-1}$ where MW_{phage} is the molecular weight of wild-type M13 phage (1.64 x 10^7 g mol^{-1})[141] and N_A is Avogadro's number (6.02 x 10^{23} mol^{-1}). As the molecular weight of M13 phage is proportional to ssDNA (6407 bases for the wild-type phage), the final equation for number of phage particles per volume was calculated based on the following equation: (OD_{269} – OD_{320}) × 6 × 10^{16} / (number of DNA base). The phage titer was calculated by dividing the phage number by the culture media volume.

Fabrication of phage-templated cathode. Metal nanofoam current collectors were synthesized following a procedure previously described, with the following modifications[96]. The 10^{13} phage particles/mL solution in PBS buffer was prepared as described above. Substrates for electrode samples were cleaned by immersing electrode spacers (Pred Materials International, SUS316L) in 18 M sulfuric acid (VWR, 470302-872) for 30 min followed by thorough rinsing with DI water. Substrates for additional samples were prepared by cutting glass slides into 0.5 cm^2 chips and treating with ozone (UV-O_3 exposure) for 10 min. To crosslink the phage, 10 μL of phage-PBS solution was

pipetted onto the substrate and enclosed in a polypropylene chamber (1 L volume) with 20 mL excess DI in order to maintain humidity for 4 hr. Samples were then removed and allowed to sit in 0.2 mL 50% glutaraldehyde (Sigma Aldrich, 340855) under ambient conditions for 8 hr in order to evaporate excess liquid. These samples were rinsed 3 times with DI water in order to remove glutaraldehyde. Samples were sensitized for 30 min using 10 mM tetraamminepalladium chloride solution (Sigma Aldrich, 323438), and rinsed three times with DI water. The nickel electroless deposition solution was made in a 2,000 mL glass bottle (VWR, 10754-822) by first mixing 1,000 mL of DI water with 7.17 g sodium DL-lactate (Sigma Aldrich, L4263) and 20.93 g 3-(N-morpholino) propanesulfonic Acid (MOPS, Sigma Aldrich, 69947) and adjusting the pH to 7.0 using sodium hydroxide (Sigma Aldrich, S8045). Nickel sulfate hexahydrate (Sigma Aldrich, 227676) (8.411 g) was added and dissolved by stirring, followed by the addition of 3.948 g borane dimethylamine (Sigma Aldrich, 180238). Samples were exposed to the electroless deposition solution for 45 min, followed by rinsing three times with DI water. The sample is then dried under ambient conditions.

Deposition of manganese oxide active material.   An electrodeposition solution of 0.1 M manganese acetate (Sigma Aldrich, 221007) and 0.1 M sodium sulfate (Sigma Aldrich, 239313) was prepared and kept in a glass bottle. Nickel current collectors were fabricated as described in the previous section and then heated in air in a small box furnace (MTI Corporation, KSL1200XJF, 6 °C / min ramp followed by holding at 350 °C for 30 min). The nickel current collectors were weighed following heating. The back of the sample was covered with Kapton tape (Uline, S-11730) in order to block deposition. The sample, Pt counter electrode (Millipore Sigma 298093) and reference electrode (Ag/AgCl, BASi MF-2052) were placed in a 3-electrode setup using 50 mL of deposition solution. Electrodeposition was performed using a potentiostat (BioLogic VMP3) by maintaining -1.8 V versus the counter electrode for 15 min (-1.0 V versus reference electrode). Samples were then washed three times using DI water, allowed to dry and heated in air in a box furnace (6 °C min^{-1} ramp followed by holding at 350 °C for 30 min). As-deposited manganese hydroxide films were

19

golden brown and turned black upon conversion to manganese oxide during heating, forming the Ni–MnO$_x$ electrode. The nickel current collector weight was subtracted from the final weight of the Ni–MnO$_x$ electrode samples in order to determine the active material mass.

Calculation of porosity.   The porosities of nanofoams were calculated from SEM images. Grayscale images were loaded into FIJI/ImageJ and processed using the thresholding function (Image > Adjust > Threshold). The B&W setting was selected such that nanofoam struts would appear white and the background would appear black. The 'Auto' setting was used to automatically choose a thresholding value that typically divided a bimodal brightness distribution between a bright foreground and a dark background. Following thresholding, the resulting average pixel value was measured (with Analyze > Set Measurements, select Limit to threshold setting enabled, the average pixel brightness was measured with Analyze > Measure). This pixel value was divided by the maximum brightness of 255 to achieve the fraction of the image occupied by nickel nanowires on a scale of 0 to 1 (in which 1 is 100% strut and zero porosity). The porosity was calculated by subtracting this value from 1. This analysis was performed on images from each condition, and the average porosity was calculated from these values.

Battery testing.   Electrochemical cycling tests were performed in CR2016 coin cells (Pred Materials International) assembled in an Argon glovebox (Mbraun; Airgas AR UHP300). Biotemplated Ni–MnO$_x$ electrode samples were dried overnight under vacuum at 80°C for use as cathodes. These samples were placed on the coin cell casing spring and 30 μL electrolyte (1M LiPF$_6$ in 1:1 EC:DMC, Sigma Aldrich 746711) was added. Two pieces of 11/16" diameter separator (Celgard 3501) and a 9/16" diameter piece of Li foil (Alfa 15424745) were added and the coin cell was sealed using a digital pressure-controlled crimper (MTI, MSK-160E). Samples were removed from the glovebox and electrochemically cycled using a potentiostat (Biologic VMP3). For cycling tests, the rates were

20

calculated using the active material mass measure and using a theoretical capacity of 147 mAh/g. Samples were charged to 4.4 V, and then discharged at varying rates (Supplementary Figure 10) to a lower voltage cutoff of 2 V. During cycling, discharge at a given rate was performed for up to 6 cycles (Supplementary Figure 12). The measured specific capacity at a given rate was the total discharge capacity over this voltage range divided by the active material mass. Three cycles were performed at each rate and averaged to calculate the discharge capacity.

Reference

[1] L. L. Ren, S. M. Cui, F. C. Cao, Q. H. Guo, *Angew. Chem. Int. Ed.* **2014**, 53, 10147.
[2] A. S. Dorcheh, M. H. Abbasi, *J. Mater. Process. Technol.* **2008**, 199, 10.
[3] J. H. Zou, J. H. Liu, A. S. Karakoti, A. Kumar, D. Joung, Q. A. Li, S. I. Khondaker, S. Seal, L. Zhai, *ACS Nano* **2010**, 4, 7293.
[4] R. L. Liu, L. Wan, S. Q. Liu, L. X. Pan, D. Q. Wu, D. Y. Zhao, *Adv. Funct. Mater.* **2015**, 25, 526.
[5] X. Xu, H. Li, Q. Q. Zhang, H. Hu, Z. B. Zhao, J. H. Li, J. Y. Li, Y. Qiao, Y. Gogotsi, *ACS Nano* **2015**, 9, 3969.
[6] C. Zhu, T. Y. J. Han, E. B. Duoss, A. M. Golobic, J. D. Kuntz, C. M. Spadaccini, M. A. Worsley, *Nature Communications* **2015**, 6.
[7] Z. C. Wang, R. B. Wei, J. W. Gu, H. Liu, C. T. Liu, C. J. Luo, J. Kong, Q. Shao, N. Wang, Z. H. Guo, X. B. Liu, *Carbon* **2018**, 139, 1126.
[8] M. A. Worsley, P. J. Pauzauskie, T. Y. Olson, J. Biener, J. H. Satcher, T. F. Baumann, *Journal of the American Chemical Society* **2010**, 132, 14067.
[9] G. S. Wei, Y. S. Liu, X. X. Zhang, F. Yu, X. Z. Du, *Int. J. Heat Mass Transfer* **2011**, 54, 2355.
[10] Z. Xu, Y. Zhang, P. G. Li, C. Gao, *ACS Nano* **2012**, 6, 7103.
[11] S. B. Ye, J. C. Feng, P. Y. Wu, *ACS Applied Materials & Interfaces* **2013**, 5, 7122.
[12] Y. Tang, S. Gong, Y. Chen, L. W. Yap, W. L. Cheng, *ACS Nano* **2014**, 8, 5707.
[13] Q. Q. Zhang, X. Xu, H. Li, G. P. Xiong, H. Hu, T. S. Fisher, *Carbon* **2015**, 93, 659.
[14] M. Yang, N. F. Zhao, Y. Cui, W. W. Gao, Q. Zhao, C. Gao, H. Bai, T. Xie, *ACS Nano* **2017**, 11, 6817.
[15] S. Han, D. Q. Wu, S. Li, F. Zhang, X. L. Feng, *Adv. Mater.* **2014**, 26, 849.
[16] D. B. Le, S. Passerini, J. Guo, J. Ressler, B. B. Owens, W. H. Smyrl, *J. Electrochem. Soc.* **1996**, 143, 2099.
[17] D. Kalpana, K. S. Omkumar, S. S. Kumar, N. G. Renganathan, *Electrochim. Acta* **2006**, 52, 1309.
[18] G. R. Li, Z. P. Feng, Y. N. Ou, D. C. Wu, R. W. Fu, Y. X. Tong, *Langmuir* **2010**, 26, 2209.

[19]   X. T. Zhang, Z. Y. Sui, B. Xu, S. F. Yue, Y. J. Luo, W. C. Zhan, B. Liu, *J. Mater. Chem.* **2011**, 21, 6494.

[20]   P. Hao, Z. H. Zhao, J. Tian, H. D. Li, Y. H. Sang, G. W. Yu, H. Q. Cai, H. Liu, C. P. Wong, A. Umar, *Nanoscale* **2014**, 6, 12120.

[21]   P. Cheng, T. Li, H. Yu, L. Zhi, Z. H. Liu, Z. B. Lei, *Journal of Physical Chemistry C* **2016**, 120, 2079.

[22]   H. Q. Li, P. He, Y. G. Wang, E. Hosono, H. S. Zhou, *J. Mater. Chem.* **2011**, 21, 10999.

[23]   H. W. Liang, Z. Y. Wu, L. F. Chen, C. Li, S. H. Yu, *Nano Energy* **2015**, 11, 366.

[24]   B. Wang, W. Al Abdulla, D. L. Wang, X. S. Zhao, *Energy & Environmental Science* **2015**, 8, 869.

[25]   H. Gao, T. F. Zhou, Y. Zheng, Y. Q. Liu, J. Chen, H. K. Liu, Z. P. Guo, *Advanced Energy Materials* **2016**, 6.

[26]   Y. Wang, D. Z. Kong, W. H. Shi, B. Liu, G. J. Sim, Q. Ge, H. Y. Yang, *Advanced Energy Materials* **2016**, 6.

[27]   G. M. Zhou, E. Paek, G. S. Hwang, A. Manthiram, *Advanced Energy Materials* **2016**, 6.

[28]   L. L. Fan, X. F. Li, X. S. Song, N. N. Hu, D. B. Xiong, A. Koo, X. L. Sun, *ACS Applied Materials & Interfaces* **2018**, 10, 2637.

[29]   D. Saikia, Y. W. Chen-Yang, Y. T. Chen, Y. K. Li, S. I. Lin, *Desalination* **2008**, 234, 24.

[30]   F. B. Hao, Z. W. Zhang, L. W. Yin, *ACS Applied Materials & Interfaces* **2013**, 5, 8337.

[31]   S. J. Shi, J. P. Tu, Y. Y. Tang, Y. Q. Zhang, X. L. Wang, C. D. Gu, *J. Power Sources* **2013**, 240, 140.

[32]   M. A. Garakani, S. Abouali, B. Zhang, C. A. Takagi, Z. L. Xu, J. Q. Huang, J. Q. Huang, J. K. Kim, *ACS Applied Materials & Interfaces* **2014**, 6, 18971.

[33]   Q. Y. An, Y. F. Li, H. D. Yoo, S. Chen, Q. Ru, L. Q. Mai, Y. Yao, *Nano Energy* **2015**, 18, 265.

[34]   Y. Xie, Z. Meng, T. W. Cai, W. Q. Han, *ACS Applied Materials & Interfaces* **2015**, 7, 25202.

[35]   J. R. He, Y. F. Chen, W. G. Lv, K. C. Wen, C. Xu, W. L. Zhang, W. Qin, W. D. He, *ACS Energy Letters* **2016**, 1, 820.

[36]   J. Q. Huang, Z. Y. Wang, Z. L. Xu, W. G. Chong, X. Y. Qin, X. Y. Wang, J. K. Kim, *ACS Applied Materials & Interfaces* **2016**, 8, 28663.

[37]   W. H. Chen, S. H. Qi, L. Q. Guan, C. T. Liu, S. Z. Cui, C. Y. Shen, L. W. Mi, *J. Mater. Chem. A* **2017**, 5, 5332.

[38]   X. H. Tian, Y. K. Zhou, X. F. Tu, Z. T. Zhang, G. D. Du, *J. Power Sources* **2017**, 340, 40.

[39]   Z. Y. Sui, C. Y. Wang, K. W. Shu, Q. S. Yang, Y. Ge, G. G. Wallace, B. H. Han, *J. Mater. Chem. A* **2015**, 3, 10403.

[40]   Z. Y. Ma, H. L. Cao, X. F. Zhou, W. Deng, Z. P. Liu, *Rsc Advances* **2017**, 7, 15857.

[41]   L. W. Yin, Z. W. Zhang, Z. Q. Li, F. B. Hao, Q. Li, C. X. Wang, R. H. Fan, Y. X. Qi, *Adv. Funct. Mater.* **2014**, 24, 4176.

[42]   J. K. Meng, Y. Cao, Y. Suo, Y. S. Liu, J. M. Zhang, X. C. Zheng, *Electrochim. Acta* **2015**, 176, 1001.

[43]   Y. Tang, H. Q. Wang, D. F. Hou, H. Tan, M. B. Yang, *J. Appl. Polym. Sci.* **2020**, 137, e49127.

[44]   J. H. Huang, X. Huang, M. He, B. N. Zhang, G. Z. Feng, G. Q. Yin, Y. D. Cui, *RSC Advances* **2019**, 9, 21155.

[45]   B. Shanmugam, P. Ignacimuthu, S. Nallani, *Appl. Surf. Sci.* **2019**, 498.

[46]   S. Meng, J. Y. Zhang, W. Xu, W. P. Chen, L. P. Zhu, Z. Zhou, M. F. Zhu, *Science China Technological Sciences* **2019**, 62, 958.

[47]   H. Tamon, T. Sone, M. Okazaki, *J. Colloid Interface Sci.* **1997**, 188, 162.

[48]   W. Liao, H. B. Zhao, Z. G. Liu, S. M. Xu, Y. Z. Wang, *Composites Part B-Engineering* **2019**, 173.

[49]   X. Y. Zhu, C. Yang, P. W. Wu, Z. Q. Ma, Y. Y. Shang, G. Z. Bai, X. Y. Liu, G. Chang, N. Li, J. J. Dai, X. T. Wang, H. L. Zhang, *Nanoscale* **2020**, 12, 4882.

[50]   X. S. Ge, Y. N. Shan, L. Wu, X. D. Mu, H. Peng, Y. J. Jiang, *Carbohydr. Polym.* **2018**, 197, 277.

[51]   P. Brown, D. U. Cearnaigh, E. K. Fung, L. J. Hope-Weeks, *J. Sol-Gel Sci. Technol.* **2012**, 61, 104.

[52]   S. M. Jung, J. F. Qi, D. Oh, A. Belcher, J. Kong, *Adv. Funct. Mater.* **2017**, 27.

[53]   K. T. Nam, D. W. Kim, P. J. Yoo, C. Y. Chiang, N. Meethong, P. T. Hammond, Y. M. Chiang, A. M. Belcher, *Science* **2006**, 312, 885.

[54]   Y. J. Lee, H. Yi, W. J. Kim, K. Kang, D. S. Yun, M. S. Strano, G. Ceder, A. M. Belcher, *Science* **2009**, 324, 1051.

[55]   X. N. Dang, H. J. Yi, M. H. Ham, J. F. Qi, D. S. Yun, R. Ladewski, M. S. Strano, P. T. Hammond, A. M. Belcher, *Nature Nanotechnology* **2011**, 6, 377.

[56]   B. Neltner, B. Peddie, A. Xu, W. Doenlen, K. Durand, D. S. Yun, S. Speakman, A. Peterson, A. Belcher, *ACS Nano* **2010**, 4, 3227.

[57]   N. M. D. Courchesne, M. T. Klug, P. Y. Chen, S. E. Kooi, D. S. Yun, N. Hong, N. X. Fang, A. M. Belcher, P. T. Hammond, *Adv. Mater.* **2014**, 26, 3398.

[58]   D. Ghosh, Y. Lee, S. Thomas, A. G. Kohli, D. S. Yun, A. M. Belcher, K. A. Kelly, *Nature Nanotechnology* **2012**, 7, 677.

[59]   H. J. Yi, D. Ghosh, M. H. Ham, J. F. Qi, P. W. Barone, M. S. Strano, A. M. Belcher, *Nano Lett.* **2012**, 12, 1176.

[60]   S. W. Lee, C. B. Mao, C. E. Flynn, A. M. Belcher, *Science* **2002**, 296, 892.

[61]   C. E. Flynn, C. B. Mao, A. Hayhurst, J. L. Williams, G. Georgiou, B. Iverson, A. M. Belcher, *J. Mater. Chem.* **2003**, 13, 2414.

[62]   S. W. Lee, S. K. Lee, A. M. Belcher, *Adv. Mater.* **2003**, 15, 689.

[63]   B. D. Reiss, C. B. Mao, D. J. Solis, K. S. Ryan, T. Thomson, A. M. Belcher, *Nano Lett.* **2004**, 4, 1127.

[64]   A. B. Sanghvi, K. P. H. Miller, A. M. Belcher, C. E. Schmidt, *Nature Materials* **2005**, 4, 496.

[65]   S. K. Lee, D. S. Yun, A. M. Belcher, *Biomacromolecules* **2006**, 7, 14.

[66]   P. J. Yoo, K. T. Nam, J. F. Qi, S. K. Lee, J. Park, A. M. Belcher, P. T. Hammond, *Nature Materials* **2006**, 5, 234.

[67]   D. Y. Oh, X. N. Dang, H. J. Yi, M. A. Allen, K. Xu, Y. J. Lee, A. M. Belcher, *Small* **2012**, 8, 1006.

[68]   J. L. Wang, L. Wang, M. Y. Yang, Y. Zhu, A. Tomsia, C. B. Mao, *Nano Lett.* **2014**, 14, 6850.

[69]   H. K. Lee, Y. Lee, H. Kim, H. E. Lee, H. Chang, K. T. Nam, D. H. Jeong, J. Chung, *ACS Synthetic Biology* **2017**, 6, 1635.

[70]   K. Heo, H. E. Jin, H. Kim, J. H. Lee, E. Wang, S. W. Lee, *Nano Energy* **2019**, 56, 716.

[71]   W. C. Records, S. Y. Wei, A. M. Belcher, *Small* **2019**, 15.

[72]   G. R. Zhang, S. Y. Wei, A. M. Belcher, *ACS Applied Nano Materials* **2018**, 1, 5631.

[73]   W. C. Records, Y. Yoon, J. F. Ohmura, N. Chanut, A. M. Belcher, *Nano Energy* **2019**, 58, 167.

[74]   E. Barry, D. Beller, Z. Dogic, *Soft Matter* **2009**, 5, 2563.

[75]   H. Qi, H. Q. Lu, H. J. Qiu, V. Petrenko, A. H. Liu, *J. Mol. Biol.* **2012**, 417, 129.

[76]   R. M. Zadegan, M. D. E. Jepsen, K. E. Thomsen, A. H. Okholm, D. H. Schaffert, E. S. Andersen, V. Birkedal, J. Kjems, *ACS Nano* **2012**, 6, 10050.

[77]   S. Brown, J. Majikes, A. Martinez, T. M. Giron, H. Fennell, E. C. Samano, T. H. LaBean, *Nanoscale* **2015**, 7, 16621.

[78]   W. M. Shih, J. D. Quispe, G. F. Joyce, *Nature* **2004**, 427, 618.

[79]   J. C. Frei, J. R. Lai, in *Peptide, Protein and Enzyme Design*, Vol. 580 (Ed: V. L. Pecoraro) **2016**, p. 45.

[80]   L. Chasteen, J. Ayriss, P. Pavlik, A. R. M. Bradbury, *Nucleic Acids Res.* **2006**, 34.

[81]   T. F. Meyer, K. Geider, *J. Biol. Chem.* **1979**, 254, 2642.

[82]   K. Geider, I. Baumel, T. F. Meyer, *J. Biol. Chem.* **1982**, 257, 6488.

[83]   T. F. Meyer, K. Geider, *Nature* **1982**, 296, 828.

[84]   G. Harth, I. Baumel, T. F. Meyer, K. Geider, *Eur. J. Biochem.* **1981**, 119, 663.

[85]   K. Geider, *Journal of General Virology* **1986**, 67, 2287.

[86]   J. Lopez, R. E. Webster, *Virology* **1983**, 127, 177.

[87]   S. Sattar, N. J. Bennett, W. X. Wen, J. M. Guthrie, L. F. Blackwell, J. F. Conway, J. Rakonjac, *Frontiers in Microbiology* **2015**, 6.

[88]   P. M. Nafisi, T. Aksel, S. M. Douglas, *Synthetic Biology* **2018**, 3.

[89]   T. R. Shepherd, R. R. Du, H. Huang, E. C. Wamhoff, M. Bathe, *Scientific Reports* **2019**, 9.

[90]   F. A. S. Engelhardt, F. Praetorius, C. H. Wachauf, G. Bruggenthies, F. Kohler, B. Kick, K. L. Kadletz, P. N. Pham, K. L. Behler, T. Gerling, H. Dietz, *ACS Nano* **2019**, 13, 5015.

[91]   L. Specthrie, E. Bullitt, K. Horiuchi, P. Model, M. Russel, L. Makowski, *J. Mol. Biol.* **1992**, 228, 720.

[92]   M. Hu, X. L. Pang, Z. Zhou, *J. Power Sources* **2013**, 237, 229.

[93]   H. B. Lin, Y. M. Zhang, J. N. Hu, Y. T. Wang, L. D. Xing, M. Q. Xu, X. P. Li, W. S. Li, *J. Power Sources* **2014**, 257, 37.

[94]   G. Q. Liu, L. Wen, Y. M. Liu, *J. Solid State Electrochem.* **2010**, 14, 2191.

[95]   B. Z. Li, L. D. Xing, M. Q. Xu, H. B. Lin, W. S. Li, *Electrochem. Commun.* **2013**, 34, 48.

[96]   J. F. Ohmura, F. J. Burpo, C. J. Lescott, A. Ransil, Y. Yoon, W. C. Records, A. M. Belcher, *Nanoscale* **2019**, 11, 1091.

[97]   D. Oh, J. F. Qi, Y. C. Lu, Y. Zhang, Y. Shao-Horn, A. M. Belcher, *Nature Communications* **2013**, 4.

[98]   M. Russel, P. Model, *Journal of Virology* **1989**, 63, 3284.

[99]   K. A. Noren, C. J. Noren, *Methods* **2001**, 23, 169.

[100]   G. P. Dotto, K. Horiuchi, N. D. Zinder, *Proceedings of the National Academy of Sciences, USA* **1982**, 79, 7122.

[101]   K. Horiuchi, *Genes to Cells* **1997**, 2, 425.

[102]   A. Casini, F. Y. Chang, R. Eluere, A. M. King, E. M. Young, Q. M. Dudley, A. Karim, K. Pratt, C. Bristol, A. Forget, A. Ghodasara, R. Warden-Rothman, R. Gan, A. Cristofaro, A. E. Borujeni, M. H. Ryu, J. Li, Y. C. Kwon, H. Wang, E. Tatsis, C. Rodriguez-Lopez, S. O'Connor, M. H. Medema, M. A. Fischbach, M. C. Jewett, C. Voigt, D. B. Gordon, *Journal of the American Chemical Society* **2018**, 140, 4302.

[103]   A. Brunet, C. Tardin, L. Salome, P. Rousseau, N. Destainville, M. Manghi, *Macromolecules* **2015**, 48, 3641.

[104]   S. M. Jung, H. Y. Jung, M. S. Dresselhaus, Y. J. Jung, J. Kong, *Scientific Reports* **2012**, 2.

[105]   D. C. Lin, E. K. Dimitriadis, F. Horkay, *Journal of Biomechanical Engineering-Transactions of the ASME* **2007**, 129, 430.

[106]   R. W. Stark, T. Drobek, M. Weth, J. Fricke, W. M. Heckl, *Ultramicroscopy* **1998**, 75, 161.

[107]   S. Cardenas-Perez, J. J. Chanona-Perez, J. V. Mendez-Mendez, I. Arzate-Vazquez, J. D. Hernandez-Varela, N. G. Vera, *Trends in Food Science & Technology* **2019**, 87, 59.

[108]   Q. Liu, Z. X. Lu, M. Zhu, Z. S. Yuan, Z. Y. Yang, Z. J. Hu, J. N. Li, *Soft Matter* **2014**, 10, 6266.

[109]   L. D. Gelb, *Journal of Physical Chemistry C* **2007**, 111, 15792.

[110]   Z. X. Lu, C. G. Zhang, Q. Liu, Z. Y. Yang, *Journal of Physics D-Applied Physics* **2011**, 44.

[111]   Z. X. Lu, M. Zhu, Q. Liu, *Journal of Physics D-Applied Physics* **2014**, 47.

[112]   X. Q. Feng, R. Xia, X. Li, B. Li, *Appl. Phys. Lett.* **2009**, 94.

[113]   D. W. Liu, Q. F. Zhang, P. Xiao, B. B. Garcia, Q. Guo, R. Champion, G. Z. Cao, *Chem. Mater.* **2008**, 20, 1376.

[114]   H. G. Zhang, X. D. Yu, P. V. Braun, *Nature Nanotechnology* **2011**, 6, 277.

[115]   A. R. West, H. Kawai, H. Kageyama, M. Tabuchi, M. Nagata, H. Tukamoto, *J. Mater. Chem.* **2001**, 11, 1662.

[116]   J. J. Xu, H. Ye, G. Jain, J. S. Yang, *Electrochem. Commun.* **2004**, 6, 892.

[117]   J. Cabana, T. Valdes-Solis, M. R. Palacin, J. Oro-Sole, A. Fuertes, G. Marban, A. B. Fuertes, *J. Power Sources* **2007**, 166, 492.

[118]   A. M. Wen, N. F. Steinmetz, *Chem. Soc. Rev.* **2016**, 45, 4074.

[119]   S. A. A. Rizvi, A. M. Saleh, *Saudi Pharmaceutical Journal* **2018**, 26, 64.

[120]   Y. N. Meng, H. P. Wu, Y. J. Zhang, Z. X. Wei, *J. Mater. Chem. A* **2014**, 2, 10842.

[121]   J. Lee, C. Jo, B. Park, W. Hwang, H. I. Lee, S. Yoon, J. Lee, *Nanoscale* **2014**, 6, 10147.

[122]   D. Z. Fang, C. C. Striemer, T. R. Gaborski, J. L. McGrath, P. M. Fauchet, *Nano Lett.* **2010**, 10, 3904.

[123]   E. Kim, J. Rho, S. G. Ryu, D. Hwang, Y. Lee, K. Kim, C. Grigoropoulos, *Applied Physics Express* **2019**, 12.

[124]   P. Ambhorkar, Z. J. Wang, H. Ko, S. Lee, K. I. Koo, K. Kim, D. I. Cho, *Micromachines* **2018**, 9.

[125]   N. Nitta, F. X. Wu, J. T. Lee, G. Yushin, *Mater. Today* **2015**, 18, 252.

[126]   L. E. Asp, M. Johansson, G. Lindbergh, J. Xu, D. Zenkert, *Functional Composites and Structures* **2019**, 1, 042001.

[127]   M. Q. Wang, A. Emre, S. Tung, A. Gerber, D. D. Wang, Y. D. Huang, V. Cecen, N. A. Kotov, *ACS Nano* **2019**, 13, 1107.

[128]   W. Johannisson, D. Zenkert, G. Lindbergh, *Multifunctional Materials* **2019**, 2, 035002.

[129]   H. Atsumi, A. M. Belcher, *Acs Nano* **2018**, 12, 7986.

[130]   M. H. Al-Saleh, U. Sundararaj, *Composites Part a-Applied Science and Manufacturing* **2011**, 42, 2126.

[131]   M. Mullner, S. J. Dodds, T. H. Nguyen, D. Senyschyn, C. J. H. Porter, B. J. Boyd, F. Caruso, *Acs Nano* **2015**, 9, 1294.

[132]   Z. W. Niu, M. A. Bruckman, B. Harp, C. M. Mello, Q. Wang, *Nano Research* **2008**, 1, 235.

[133]   W. J. Chung, D. Y. Lee, S. Y. Yoo, *International Journal of Nanomedicine* **2014**, 9, 5825.

[134]   H. E. Jin, R. Farr, S. W. Lee, *Biomaterials* **2014**, 35, 9236.

[135]   C. Yanischperron, J. Vieira, J. Messing, *Gene* **1985**, 33, 103.

[136]   L. R. Nyland, D. W. Maughan, *Biophys. J.* **2000**, 78, 1490.

[137]   J. Domke, M. Radmacher, *Langmuir* **1998**, 14, 3320.

[138]   F. H. Sanchez, C. E. R. Torres, M. B. F. van Raap, L. M. Zelis, *Hyperfine Interact.* **1998**, 113, 269.

[139]   J. Sambrook, D. W. Russell, *Molecular cloning: a laboratory manual*, Cold Spring Harbor
        Laboratory Press, Cold Spring Harbor, N.Y. **2001**.

[140]   S. A. Berkowitz, L. A. Day, *J. Mol. Biol.* **1976**, 102, 531.

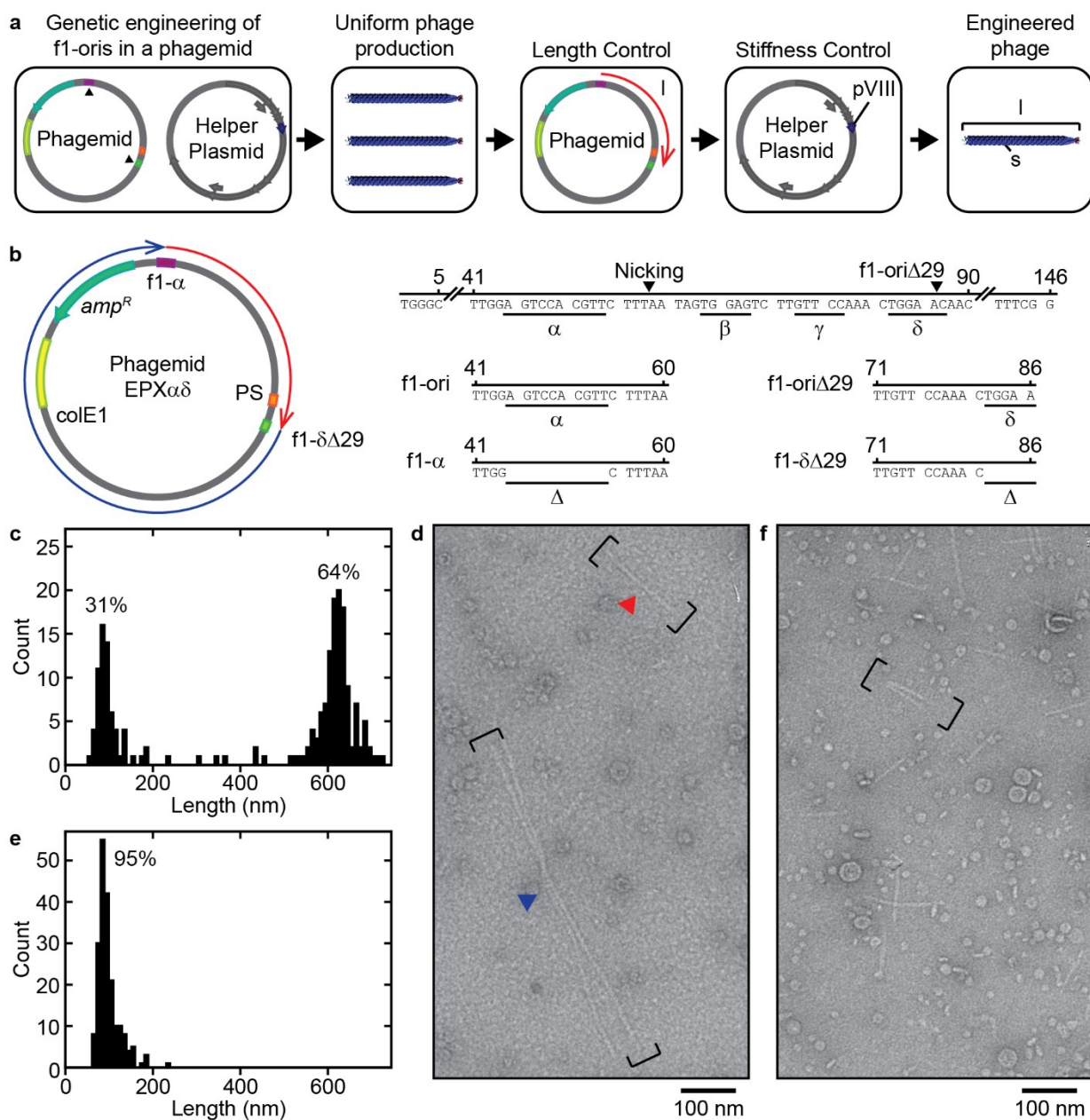[141]   J. Newman, H. L. Swinney, L. A. Day, *J. Mol. Biol.* **1977**, 116, 593.

Figures

Figure 1. Production of uniform phage of a defined length. a) The steps for the production of uniform engineered phage are shown. The black triangles show the position of f1-oris in the phagemid. The phage length (*l*) and stiffness (*s*) were controlled by tuning number of DNA between

engineered f1-oris and mutating one amino acid on pVIII, respectively. b) Engineered phagemid for the production phage of different length (Supplementary Table 1). The X in the phagemid name provides the length (number of bp) of the ssDNA. The red and blue arrows show the short (long) sequences that lead to the correct (incorrect) phage. The labels for the modified initiator (f1-α) and terminator (f1-$\delta\Delta29$) sequences are as described in the text. c) The phage length distribution obtained from the unmodified initiator and terminator (EP475). The data are from three experiments performed on different days, combined into a single distribution (N = 198). The histogram was drawn using the bin width of 10. The percent was calculated as the fraction between 50 nm and 150 nm (510 nm and 730 nm). d) An example TEM image showing a phage of correct length (red) and incorrect length (blue). e) The length distribution obtained from the modified initiator and terminator (EP475$\alpha\delta$). The data are from three experiments performed on different days, combined into a single distribution (N = 198). The histogram was drawn using the bin width of 10. f) An example TEM image showing the phage produced by EP475$\alpha\delta$ (representative example shown in the bracket).
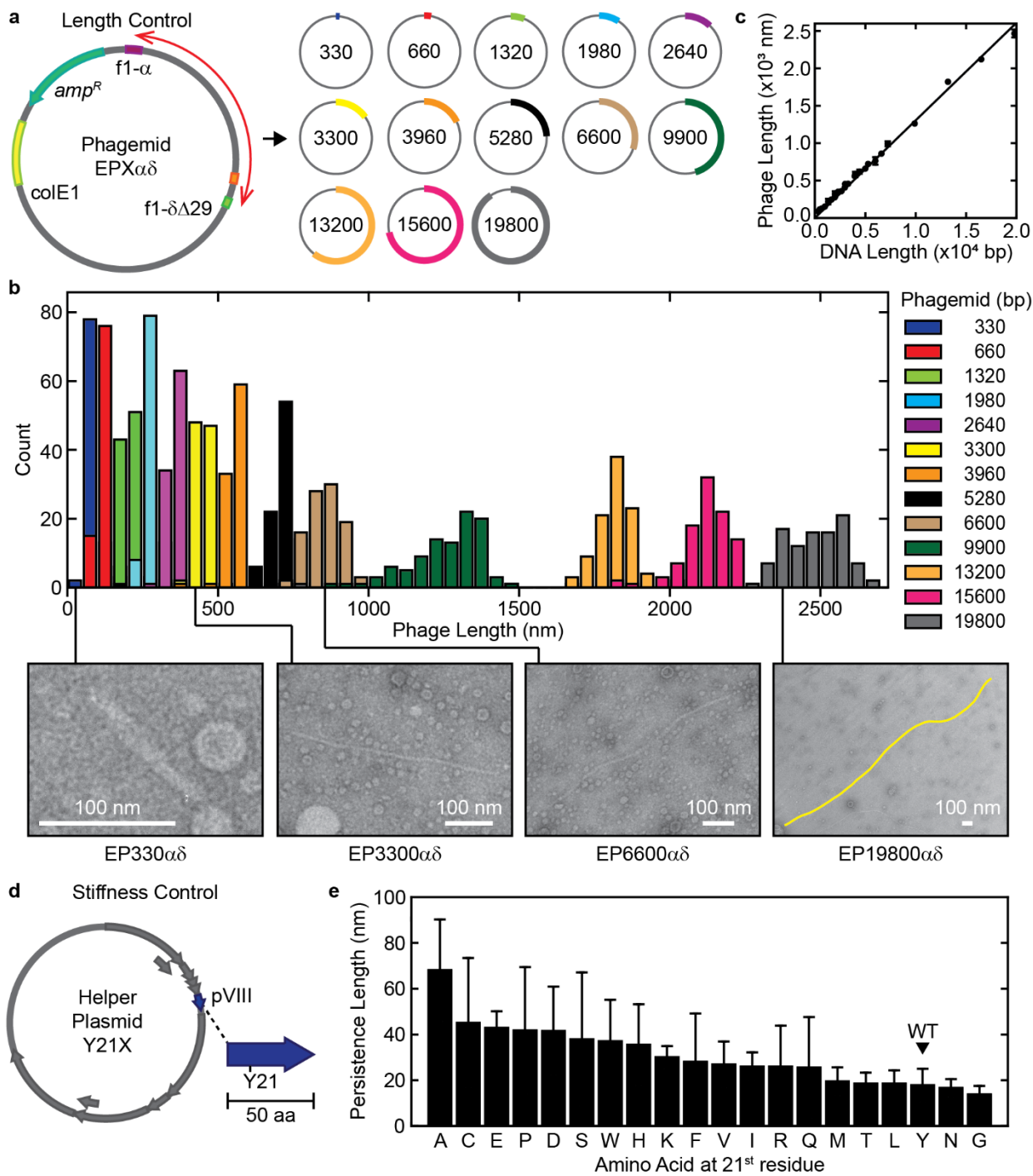
Figure 2. Independent control of phage length and stiffness. a) The set of phagemids are shown with different lengths of ssDNA (numbers are bp). The detailed plasmid map and DNA sequences are provided in Supplementary Table 2 and Supplementary Figure 14. b) The length distributions are shown for each phagemid. The data were collected from three replicates, performed on different days, and compiled to create a single distribution (N = 99). The histogram was drawn using the bin width of 50. Representative TEM images are shown four phagemids; yellow highlights the length of the largest phage. c) The relationship between mean phage length and ssDNA length. The mean is calculated from distributions obtained from three replicates performed on different days and the error bars are the standard deviations of these means. d) The helper plasmid is shown along with the location of *pVIII* and the Y21 mutation (the X in the name is the amino acid at position 21). The sequence and detailed plasmid map are provided in Supplementary Table 1 and Supplementary Figure 14. e) The phage persistence lengths measured for pVIII mutants (using EP475$\alpha\delta$). WT indicates the amino acid at position 21 of wild-type pVIII. Data are the means of three replicates performed on different days and the error bars are the standard deviations.
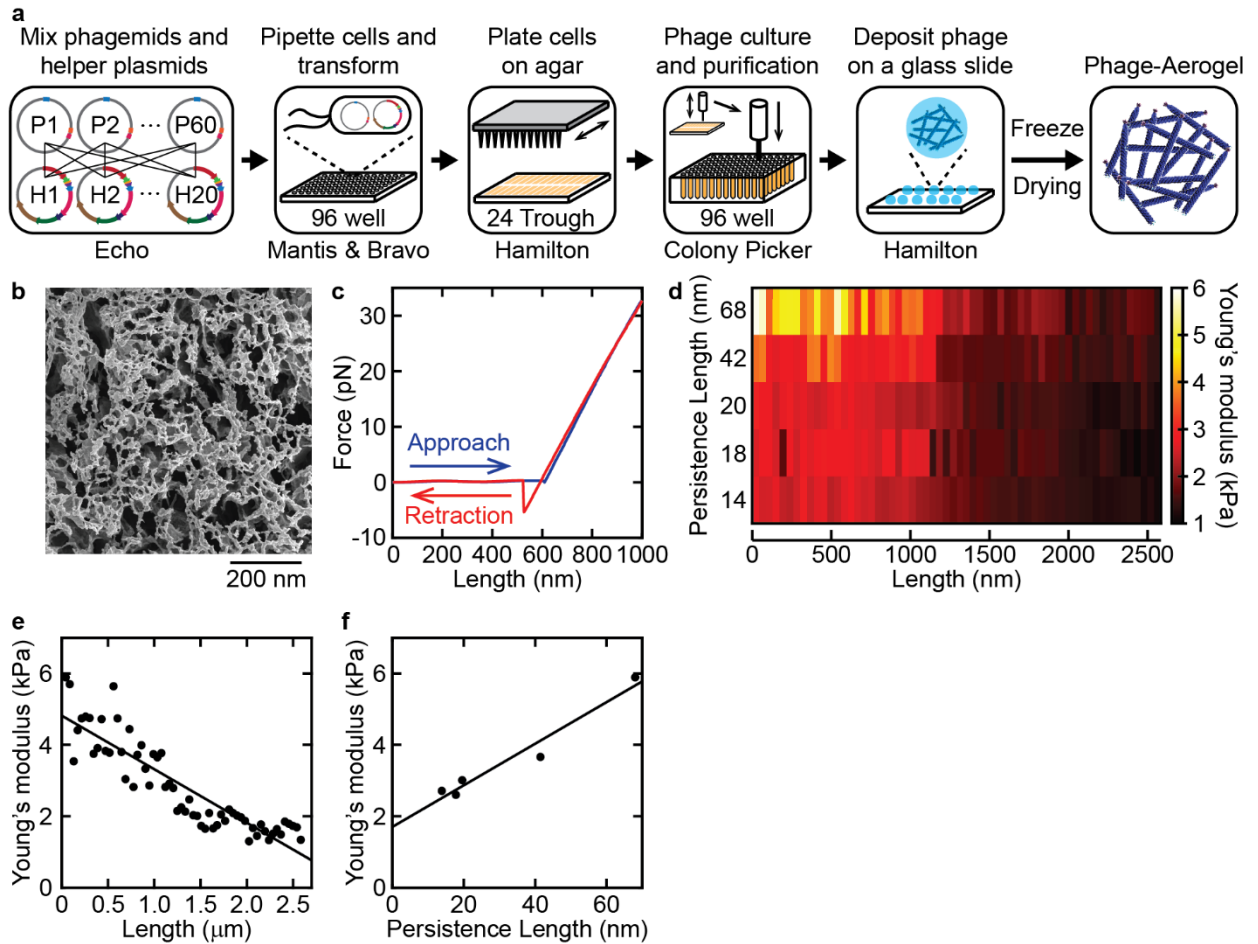
31

Figure 3. High-throughput production and characterization of aerogels. a) Steps of the high-throughput production of aerogels. Details are provided in the Methods and Supplementary Figure 6. The first step involves the mixing of different phagemids (P) and helper plasmids (H) to control length and stiffness, respectively. The high-throughput equipment used for each step are shown under the boxes. b) Representative SEM image of the phage-aerogel made from EP475$\alpha\delta$ and pVIII Y21A using the high-throughput protocol. c) Force-displacement plot of raw AFM data are shown for an aerogel made from EP660$\alpha\delta$ and pVIII Y21A. The Hertzian model is used to calculate *E* by measuring force (F) and displacement (δ). d) Three hundred samples are shown from the 1,200 phagemid/helper plasmid combination. Top to bottom (pVIII): A, D, M, Y, and G. Left to right, all 60

32

phagemids are shown. The data are representative of a single screen. e) The impact of length on Young's Modulus is shown. Each data point is the mean E for the five pVIII mutants shown in part d. f) The impact of persistence length on Young's Modulus is shown. Each data point is the mean E for the sixty lengths shown in part d.

33
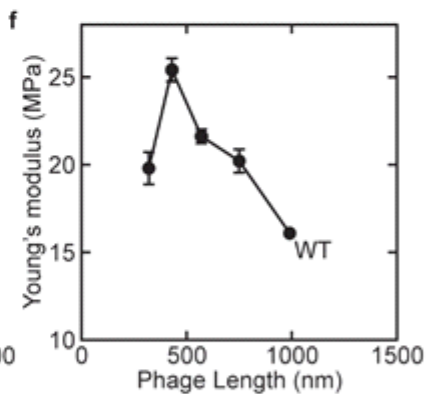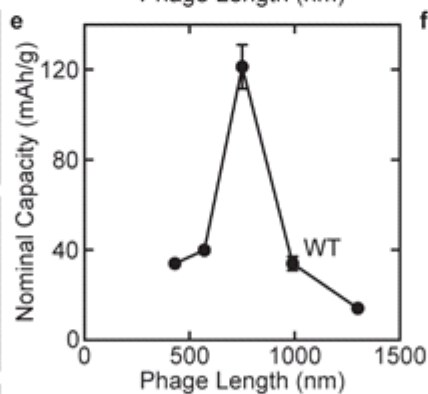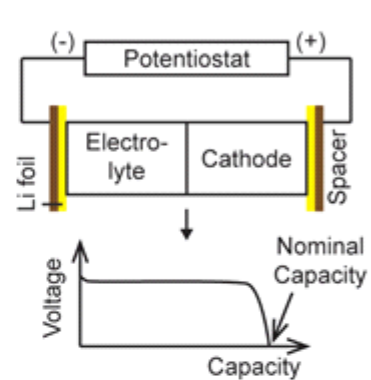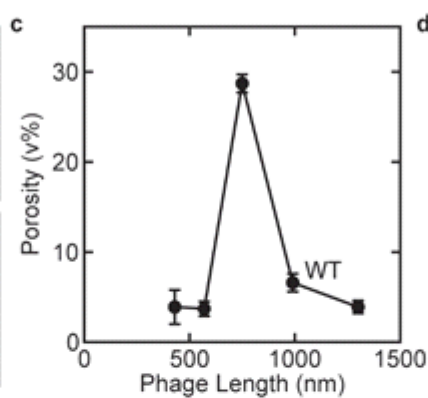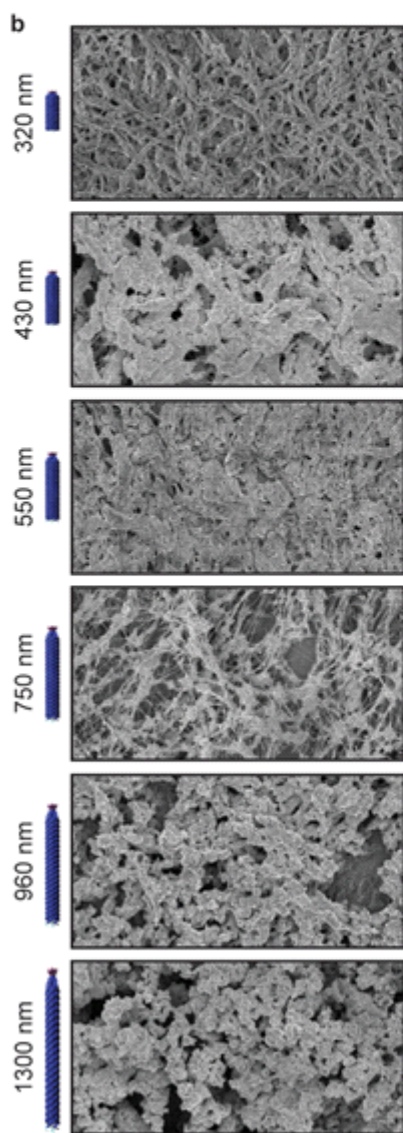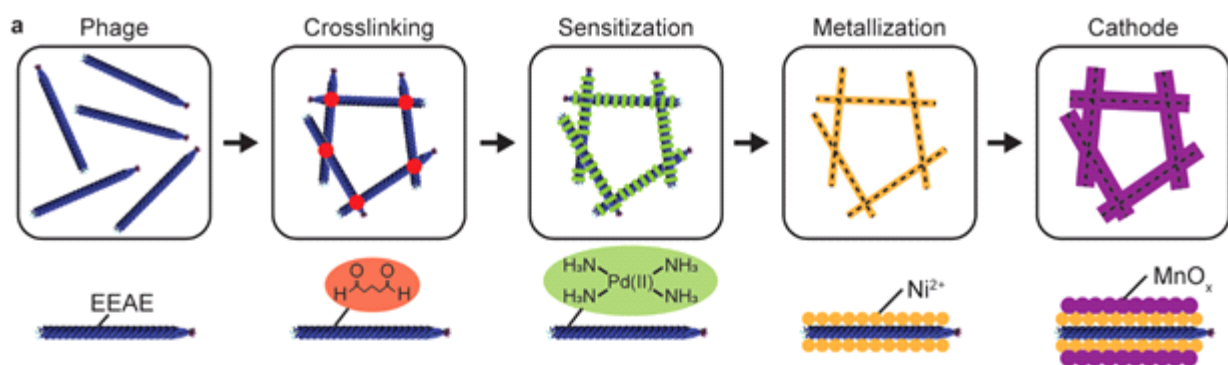
**Figure 4.** Characterization of Ni–MnO$_x$ nanofoam cathodes. a) An overview of the fabrication process is shown (Methods). The additional peptides EEAE were attached on pVIII proteins. Engineered phages were crosslinked the glutaraldehyde (red) to form hydrogels. The samples were sensitized with tetraamminepalladium chloride (green). The Ni^{2+} ions (orange) were integrated to synthesize phage-templated Ni nanofoams. After deposition of manganese oxide (purple), the phage-templated cathodes were fabricated. b) TEM images of cathodes synthesized using different lengths of engineered phage. c) Nanofoam porosity is shown as a function of the phage length used as a scaffold. For each data point, SEM images were taken at three randomly-chosen positions in a sample. Porosity was calculated from the image as described in the Methods. The error bars are the standard deviations of these measurements. d) Schematic of battery testing apparatus (Methods) and the calculation of the nominal capacity. e) Capacity dependence on the phage length used to create the nanofoam. Samples were charged to 4.4 V and discharged at varying rates to 2 V (Supplementary Figure 10). Three cycles were performed at each rate and averaged to calculate the discharge capacity. The error bars are the standard deviations of these measurements. f) The Young's moduli of the cathodes are shown as a function of phage length.
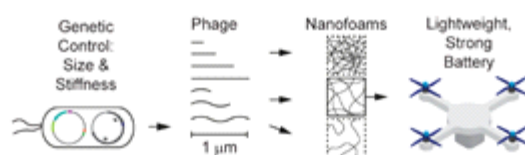
A genetically engineered phagemid system generates uniform M13 phage with controllable length and stiffness. The engineered phage are utilized as templates for synthesis of metal nanofoams (Ni-MnO$_x$), used as cathodes in Li ion batteries. By changing physical properties of M13 phage, the electrochemical and mechanical characteristics of the Ni-MnO$_x$ cathode can be controlled. This is applied towards identifying optimal cathodes to be used for structural batteries.